



Timing characteristics of Large Area Picosecond Photodetectors



B.W. Adams^a, A. Elagin^b, H.J. Frisch^b, R. Obaid^c, E. Oberla^b, A. Vostrikov^b, R.G. Wagner^a,
J. Wang^a, M. Wetstein^{b,*}

^a Argonne National Laboratory, United States

^b Enrico Fermi Institute, University of Chicago, United States

^c University of Connecticut, United States

ARTICLE INFO

Article history:

Received 26 April 2015

Accepted 12 May 2015

Available online 21 May 2015

Keywords:

MCP

TTS

LAPPD

Picosecond

Large area

Photodetector

ABSTRACT

The LAPPD Collaboration was formed to develop ultrafast large-area imaging photodetectors based on new methods for fabricating microchannel plates (MCPs). In this paper we characterize the time response using a pulsed, sub-picosecond laser. We observe single-photoelectron time resolutions of a $20\text{ cm} \times 20\text{ cm}$ MCP consistently below 70 ps, spatial resolutions of roughly 500 μm , and median gains higher than 10^7 . The RMS measured at one particular point on an LAPPD detector is 58 ps, with $\pm 1\sigma$ of 47 ps. The differential time resolution between the signal reaching the two ends of the delay line anode is measured to be 5.1 ps for large signals, with an asymptotic limit falling below 2 ps as noise-over-signal approaches zero.

© 2015 Elsevier B.V. All rights reserved.

1. Introduction

Microchannel plate photomultiplier tubes (MCP-PMTs) are compact vacuum photodetectors [1], capable of micron-scale spatial resolutions [2], sub-nanosecond time resolutions [3–5], and gains exceeding 10^7 [6]. Economical, large-area MCP photosensors with these characteristics would bring much needed timing and imaging capabilities to a wide range of applications in fields such as particle physics, nuclear physics, X-ray science, and medical imaging.

The Large Area Picosecond Photodetector (LAPPD) collaboration was formed to develop techniques for making large format ($20\text{ cm} \times 20\text{ cm}$) MCP-PMT detector systems using scalable methods and low-cost materials, addressing technical aspects of the problem from the photocathode and the gain stage to the readout electronics and vacuum packaging. Fabrication of LAPPDs is based largely on the application of thin-film materials to glass structures. In particular, a technique known as Atomic Layer Deposition (ALD) [7] enables the fabrication of large-area MCP amplification structures by conformally coating inactive, porous glass substrates [8,9]. The technique is flexible as well as scalable, allowing for the independent optimization of the geometric, resistive, and secondary electron emission properties [8] of the channel plates.

In this paper, we present an analysis of the timing characteristics for $20\text{ cm} \times 20\text{ cm}$ LAPPDTM systems. At sufficient operational voltages, we observe single-photoelectron time resolutions in the range of 50–60 ps, consistent with those of commercial MCPs with comparable pore structures. Differential time resolutions are measured as low as 5.1 ps, with the large signal limit extrapolating below 2 ps. Spatial resolutions are set by the granularity of the economical stripline anode design (see Section 2) and are measured to be less than 1 mm in both directions with respect to the stripline anodes. The median gain of the most recent MCP stack exceeds 10^7 .

1.1. Structure of this paper

Section 2 describes the essential elements of the LAPPDTM design. In Section 3 we discuss the theoretical factors that determine the time resolutions of detectors generically, and MCP detectors such as LAPPDs specifically. We also identify the key observables and dependencies to be measured. Section 4 briefly describes the setup used to measure LAPPD timing, and Section 5 describes the measurement strategy. Section 6 describes the algorithms used to construct and fit the LAPPD pulses. Section 7 describes the results; conclusions are presented in Section 8.

2. Essential elements of the LAPPDTM design

Fig. 1 shows the structure of an LAPPDTM [10]. Light is incident on a photocathode, producing photoelectrons. These accelerate

* Corresponding author.

E-mail address: matt.wetstein@gmail.com (M. Wetstein).

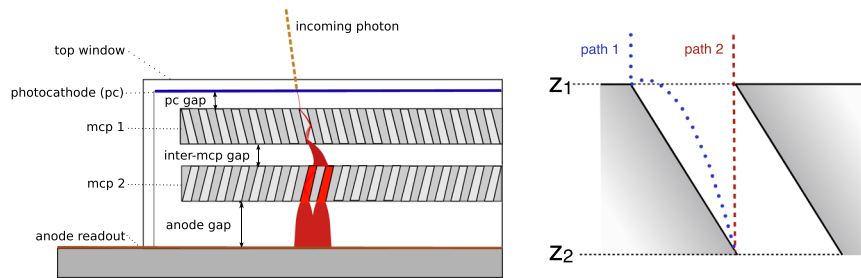


Fig. 1. Left: the structure of an LAPPD™ photomultiplier tube. Right: a schematic of photoelectrons entering the pore of an MCP. Both the dashed red and dotted blue trajectories reach height z_1 at the same time, but arrive at z_2 at different times due to different velocities and path lengths.

across a potential gap toward a pair of microchannel plates, which are high-gain structures consisting of thin plates with high secondary electron emission (SEE) enhanced, microscopic pores [1]. Voltages of roughly 1 kV are applied across each plate. Pores are oriented at 18° bias angles in opposite directions. This prevents positive ions, produced by the electron cascade in the lower plate, from reaching and damaging the photocathode. It also provides a well-defined first strike for incoming electrons. Each electron entering a pore accelerates and strikes the pore walls, starting an avalanche of secondary electrons. The avalanche builds until the amplified pulse exits the bottom of the second MCP. This electrical signal is collected on an anode structure and passed through the vacuum assembly to sampling front-end electronics, which digitize the signal at 10–15 Gsamples/second. Spacing between the MCPs is set by glass grid spacers for the data reported here [10].

Anode coverage over large areas is achieved using a 50 Ω micro-stripline design [11]. The positions of photon strikes on the photocathode are determined (i) by differential timing along the striplines, and (ii) by calculating a weighted centroid of the charge on adjacent striplines in the transverse direction. This design allows economical area coverage as the number of readout channels scales linearly with length, rather than quadratically.

3. Factors that limit and determine time resolution

The timing characteristics of these photodetectors are determined by two key aspects of the detection process:

- Jitter in the formation of avalanches within the gain stage: this is determined by the physical properties of the MCP stack, such as pore diameters and bias angles, operational voltages, spacings between the components, and SEE characteristics.
- Information loss in the transmission and recording of the signal: this includes noise, attenuation of high frequency components as the pulse travels along the striplines, and quantization effects from pulse digitization.

3.1. Jitter in the MCP signal formation, with respect to photon arrival

The amplification process in an MCP detector is subject to fluctuations in the transit of the initial photoelectron (PE) and in the evolution of the avalanche. These fluctuations introduce a jitter in the start time (t_0) and development of the MCP pulse with respect to the incoming photon. This jitter is largest for single-photoelectron pulses, independent of signal processing considerations. In the limit of many photoelectrons, it should decrease statistically.¹

¹ The exact relationship between time resolution and N_{phot} is complicated, depending on whether the photoelectrons enter one or several MCP pores, and whether the avalanche ultimately saturates.

The most significant factor driving single-PE jitter is the “first strike”. This is illustrated schematically in Fig. 1, on the right. The dotted blue and dashed red photoelectrons accelerate across the photocathode gap, typically a few hundred volts. Both PEs reach the top plate (z_1) at the same time with the same energy. The PE on the dotted blue trajectory immediately strikes the pore, while the dashed red trajectory continues deeper into the pore. A secondary electron produced at the strike-point of the dotted blue trajectory starts with $O(1)$ eV initial energy before accelerating towards z_2 . The original photoelectron on the dashed red trajectory accelerates towards z_2 over a shorter path, and starting with $O(100)$ eV energy. Thus, the dashed red trajectory arrives at position z_2 before the dotted blue one. The difference is $O(10)$ picoseconds for these two strike points. There are many more possible trajectories for secondary electrons produced along path 1, and there are many different first strike points within the pore. Given the current 20 μm diameter and 8° bias of the default LAPPD™ pores, these variations in trajectory lead to an $O(10)$ picosecond jitter in t_0 of the avalanche. However, this jitter can be reduced by shrinking the pore size. Excellent single-PE time resolutions have been achieved using MCPs with pore diameters below 10 μm [12].

The number of secondaries and the randomization of their initial directions and energies further contribute to fluctuations in the development of the avalanche. The larger $N_{secondaries}$, the more these fluctuations will average out, and the more each individual pulse will behave in accordance with the mean behavior. A key way to reduce this is to increase the photocathode gap energy so that the first strike produces a large number of secondaries and to coat the pore surface with materials optimized for high secondary electron emission [8,13].

In addition to variability from the first strike, some jitter in the time evolution of the avalanche is driven by the transition between the two MCPs of the gain stage. The avalanche from the first MCP will spread into a finite number of pores in the second-stage MCP. Depending on which pore in the first MCP is struck, fluctuations in this charge spreading will affect both the saturation and the timing of the resulting pulse.

3.2. Uncertainties in extracting the arrival time from the MCP signal

Even if an MCP provided a precisely repeatable signal with fixed t_0 , there would still be uncertainty in the arrival of that MCP signal due to limitations on extracting the signal from noise. Here we briefly discuss these issues, based largely on material from Ref. [14–16].

Fig. 2 demonstrates how the presence of noise introduces an uncertainty in the threshold crossing time of an otherwise repeatable signal. The right two plots in Fig. 2 show the dependence of the size of the timing uncertainty for a given noise level on the rise time of the signal, which defines the slope between voltage and time.

By sampling more points along the rising edge, the uncertainty in the timing of the signal goes down with \sqrt{N} , assuming that the Nyquist–Shannon condition is met. Then, the time resolution can be described by Ritt’s parameterization [15,16], shown in the following equation:

$$\Delta t = \frac{\Delta u}{U} \times \frac{t_{rise}}{\sqrt{n}} = \frac{\Delta u}{U} \times \frac{t_{rise}}{\sqrt{f_s \times t_{rise}}} = \frac{\Delta u}{U} \times \frac{\sqrt{t_{rise}}}{\sqrt{f_s}} = \frac{\Delta u}{U} \times \frac{1}{\sqrt{3f_s \times f_{3\text{ dB}}}} \quad (1)$$

where $\Delta u/U$ is the noise-over-signal, t_{rise} is the rise-time of the signal, and n is the number of samples taken along the rising edge of the signals, f_s is the sampling rate, and $f_{3\text{ dB}}$ is the highest frequency component of the pulse. The noise is assumed to be uncorrelated white noise, an assumption that might not be generically true in real life experiments.

The noise of the system is determined primarily by the design of the readout, particularly the electronics. The 15 Gsample/s PSEC4 chip developed for LAPPD™ readout has a noise per channel of 700 μV [17]. The oscilloscope measurements presented in this paper have noise levels around 3 mV. With gains above 10^7 , the LAPPD™ system is capable of achieving noise-over-signal values well below 0.001.

The rise time of the pulses is determined by the geometry and operational parameters of the MCPs, as well as the intrinsic analog bandwidth of the anode and front-end. Fig. 3 shows that the highest frequency components of the signals above noise (~ 500 MHz) are well below the analog bandwidth allowed by the anode design and readout (1.6 GHz for the PSEC4 electronics and 3 GHz for the scope) [11].

Based on these detector parameters and using Eq. (1), we estimate that the LAPPD™ readout should be capable of time resolutions approaching a single picosecond. For single-photoelectrons, the overall time resolution is dominated by the O(10) ps intrinsic jitter from the MCPs, rather than the readout. In the limit of many photoelectrons, and for future designs with optimized MCPs, improvements in time resolution will come from improvements to the readout such as higher bandwidth anodes, faster sampling rates, and lower noise electronics.

3.3. Relevant observables

The timing limitations imposed by the properties of the gain stage can be measured by studying the absolute timing of the detector in single-PE operation with respect to a photodiode triggered by the laser (see Section 4). It can be characterized by

the width of the Transit Time Spread (TTS). The limiting factor for multiple photoelectron operation is driven by the noise over signal (N/S) quality of the readout and can be measured using differential timing: the difference in arrival times of the two pulses at opposite ends of the delay line anode. In differential timing measurements, fluctuations in the start and development of the signal cancel out, leaving only the uncertainties due to noise in the readout. This observable we will refer to as the Differential Time Spread (DTS), and it improves with increasing signal size (or decreasing noise), regardless of whether the large signal is achieved by more photoelectrons or higher gains.

The timing characteristics of LAPPD™ systems will be relevant to different applications in different ways. Looking at some examples from high energy physics, water Cherenkov (WCh) detectors are single-photon counting devices; events are reconstructed using precision measurements of each individual emitted photon. The timing requirements are less demanding (< 100 ps), but the timing capabilities are more limited due to the intrinsic jitter of the gain stage on the single-PE TTS. Time-of-flight (TOF) detectors require much better time resolutions, but also look at much larger signals – typically 50 photoelectrons produced by a high energy particle traversing a radiator [14]. For these applications we are more concerned with the large-signal limits of LAPPD™ systems, determined by the readout. These large-signal resolutions can be characterized by looking at the DTS. In this paper we will discuss both the TTS and DTS, as well as their dependence on operational parameters such as voltage and S/N.

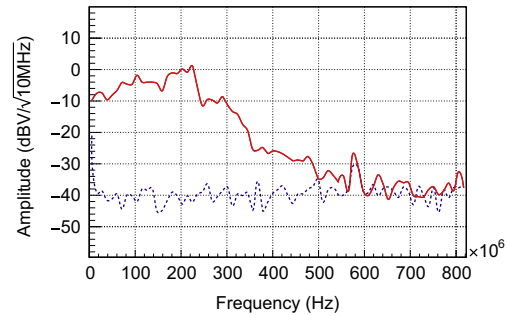


Fig. 3. Frequency spectrum of the MCP signal plus noise (solid red) overlaid on the pure noise spectrum (dashed blue). Signal dominates over noise only up to around 500 MHz.

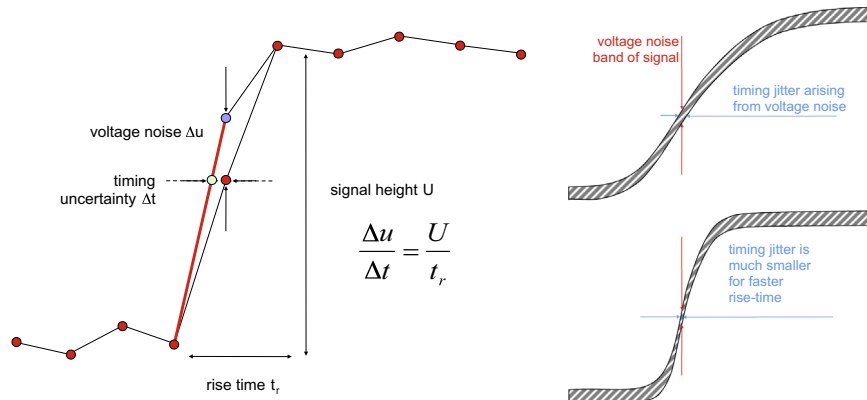


Fig. 2. Left: an illustration showing how voltage noise translates into timing uncertainty for determining the time a signal crosses a threshold. Right: two sketches showing how the impact of noise on timing also depends on the risetime of the signal.

4. Experimental setup

In this section we will briefly describe the test setup used to characterize LAPPD™ detector systems. More detailed discussions of the characterization facility can be found in Ref [18].

For all of the measurements, signals are produced by shining UV light from a sub-picosecond pulsed Ti:Sapphire laser on a thin aluminum photocathode 2 mm above the gain stage. The arrival time of the MCP pulses can therefore be measured precisely against a trigger signal derived from these laser pulses. Using a statistical technique described in Section 5, we can achieve low light intensities and study the characteristics of MCP pulses derived from single-photoelectrons. The laser spot size is roughly 1 mm, and a motorized stage is used to study the response and different locations on the detector surface. The shapes of the pulses are measured using a fast oscilloscope and written to disk for offline analysis.

This paper presents the results of two separate studies. One set of measurements was performed on an unsealed LAPPD™ detector system inserted into a larger, steel vacuum chamber (the “8-in. Chamber”) [18]. The other study was performed on a vacuum tight, resealable glass LAPPD™ detector, known as the “Demountable” [18].

4.1. The 8 in. chamber

Early studies of 8 in. microchannel plates were performed before the glass vacuum packaging for LAPPD_s was developed. A complete detector stack was assembled with proper electrical contacts, and inserted into a larger, stainless steel vacuum chamber (Fig. 4). Laser light entered the chamber through a quartz window and was directed onto the MCP stack using mirrors. Signals were brought out of the chamber through SMA feedthroughs. Due to the limited number of feedthroughs, only four striplines could be instrumented at a time. One key advantage of the 8 in. chamber was the ability to independently control the voltages at each stage of the MCP stack.

4.2. The demountable detector

The demountable assembly is an 8.66 in. x 8.66 in. glass vacuum tube detector made from LAPPD™ production parts, whose differences from the sealed detector of the design goal are that (1) the tube is actively pumped rather than hermetically sealed; (2) the seal between the fused silica top window and the tube body is with an O-ring rather than an indium seal; and (3) the photocathode is a thin aluminum layer rather than a bialkali film, as the demountable is assembled in air. Inside the demountable we place a stack of 2 ALD-functionalized 8 in. x 8 in. MCPs, with spacers in the three gaps: (a) between the MCP stack and the

anode; (b) between the two MCPs; (c) between the MCP stack and the photocathode [10]. The spacers are ALD-coated with a resistive layer. The resistances of the spacers and plates set the respective operational voltages, and allow signals to pass from the photocathode through the stack to the anode strips, which are DC terminated with 10 kΩ resistors [10]. Thus, unlike the 8 in. chamber, this voltage divider does not allow independent voltage control over each component. High voltage electrical contact is made by connecting to the aluminum side of the top-window on end-tabs where the window extends past the vacuum region of the demountable body.

5. Measurement strategy

A pulsed, sub-ps laser was used to characterize the time resolution of the large-area MCPs. Absolute timing of the MCP response was measured in relation to a fast photodiode triggered by the laser. Single-photoelectron operation was achieved by controlling photon statistics.

The average UV laser power, of order 100 nano-Watts, was sufficient to produce many photoelectrons per pulse, even with a low quantum efficiency (QE) aluminum photocathode. Without attenuation, the fraction of laser pulses with an observed MCP signal was 100%. However, the beam could be attenuated to the point where some fraction of laser pulses produced no discernible signal, as determined from the oscilloscope data using analysis techniques described in Section 6.1. Once the detector was operating in a regime where the fraction of events with good pulses was sufficiently low, the probability of producing more than one PE was statistically suppressed. Fig. 5 shows the relationship between average UV intensity and the probability of an MCP signal. The slope of this plot at low laser intensities can be used to extrapolate to higher intensities, providing a statistical handle on the number of photoelectrons. This approach does not depend on the choice of photocathode or precise knowledge of the QE.

6. Analysis techniques

6.1. Pulse selection

Pulses are separated from background on the basis of a time over threshold (TOT) cut. Pulses are identified as a region of the signal trace where the charge exceeds a predetermined threshold of 5 mV for a duration longer than 1.0 ns. We explored several possible pulse selection methods, but found this technique to be simple, robust, and effective at separating signals from white noise and RF interference from the laser. The result of this cut on the

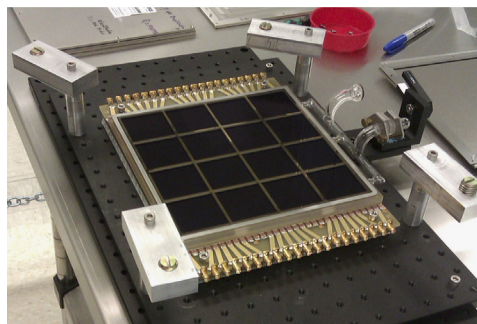
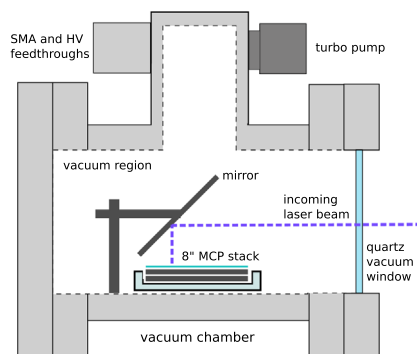


Fig. 4. Left: a schematic illustration of the 8 in. MCP test-chamber. Right: a picture of the assembled demountable LAPPD before placing and sealing the top window.

amplitude distribution of the MCP pulses is shown in Fig. 6. This analysis requires events where only one pulse is identified, although the number of events with $N_{pulses} > 1$ is negligible.

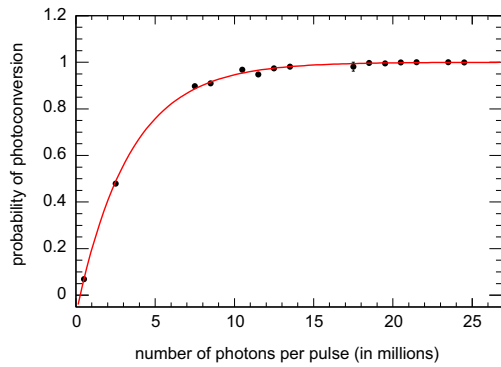


Fig. 5. Probability of the Ti:Sapphire laser pulse generating an MCP signal on the aluminum photocathode, plotted as a function of pulse energy. At sufficiently high laser intensities, this probability approaches unity; as the laser is attenuated below roughly 10 million UV photons per pulse, the fraction of laser pulses producing an MCP signal begins to drop and eventually approaches zero.

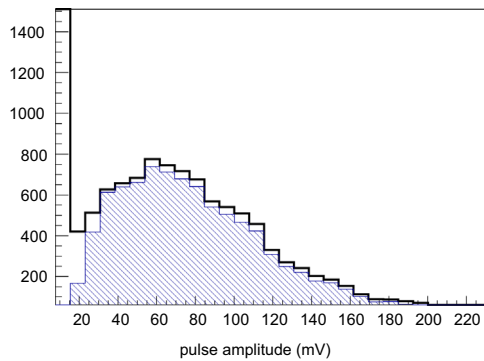


Fig. 6. The amplitude distribution of pulses from the 8 in. chamber (in thick black), showing the separation between the peak of the distribution and the pedestal near zero. The shaded blue region shows the same distribution after applying the TOT cut and requiring only one pulse.

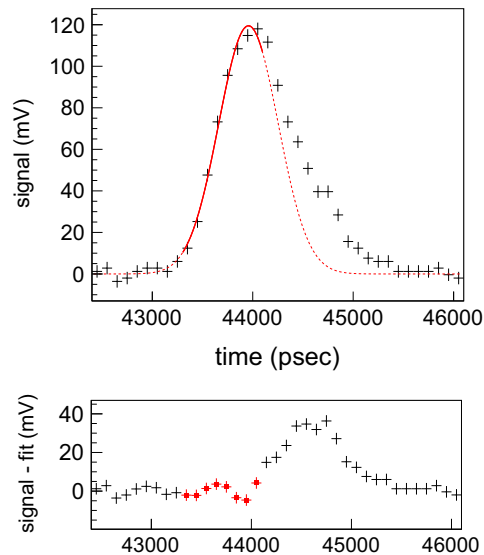
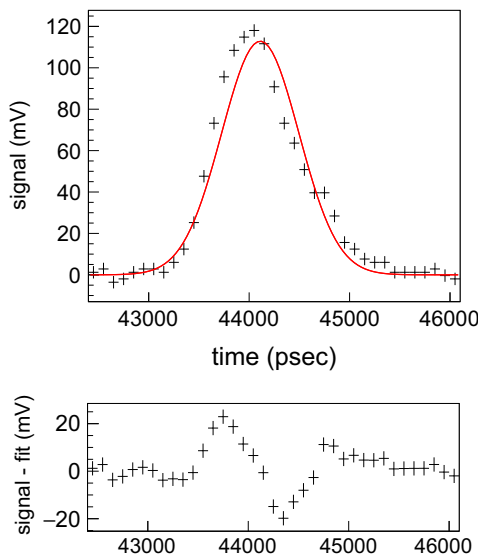


Fig. 7. Two examples of Gaussian fits to an MCP pulse, plotted above a graph showing the difference between the fitted curve and data points. The error bars correspond to 3 mV white noise on the oscilloscope. On the left plot, the pulse is fitted over the full range. The right plot shows the prescription used in the data analysis of fitting the rising edge only. The solid line and closed circles on the right correspond to the region used in the fit. The dashed line and open points are included to show the fit beyond the range of interest.

6.2. Timing algorithms

Several time reconstruction algorithms were tested : constant-fraction discrimination, fitting with a Gaussian distribution, and template fitting. These approaches are taken largely from Ref. [14].

A simple, but nonetheless effective technique for reconstructing pulse arrival times is to use a Constant-Fraction Discriminator (CFD). This technique is robust and simple, but does not capture the full information contained in the pulse shape, and it suffers from a time slewing for pulses of different shapes.

Another technique is to fit a partial range of the pulses with a Gaussian distribution. As illustrated in Fig. 7, pulse shapes from the LAPPDs are non-Gaussian. Any naive fit of a Gaussian distribution to these pulses will yield worse transit time spreads than

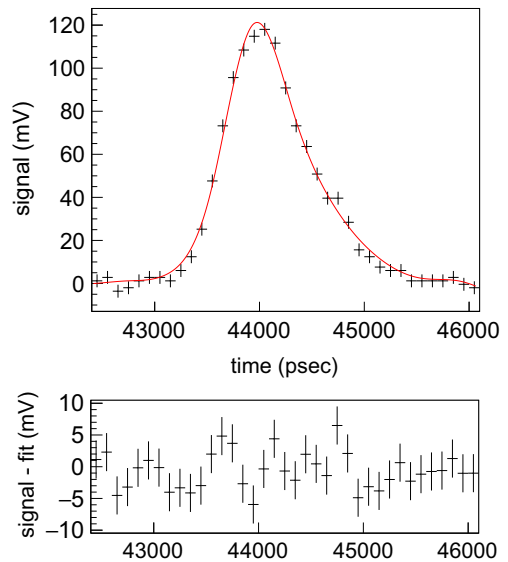


Fig. 8. Best fit of the template shape to an example pulse, plotted over the full range of the pulse. The lower plot shows the difference between each data point and the fitted curve, with 3 mV error bars corresponding to oscilloscope noise, over the range of interest.

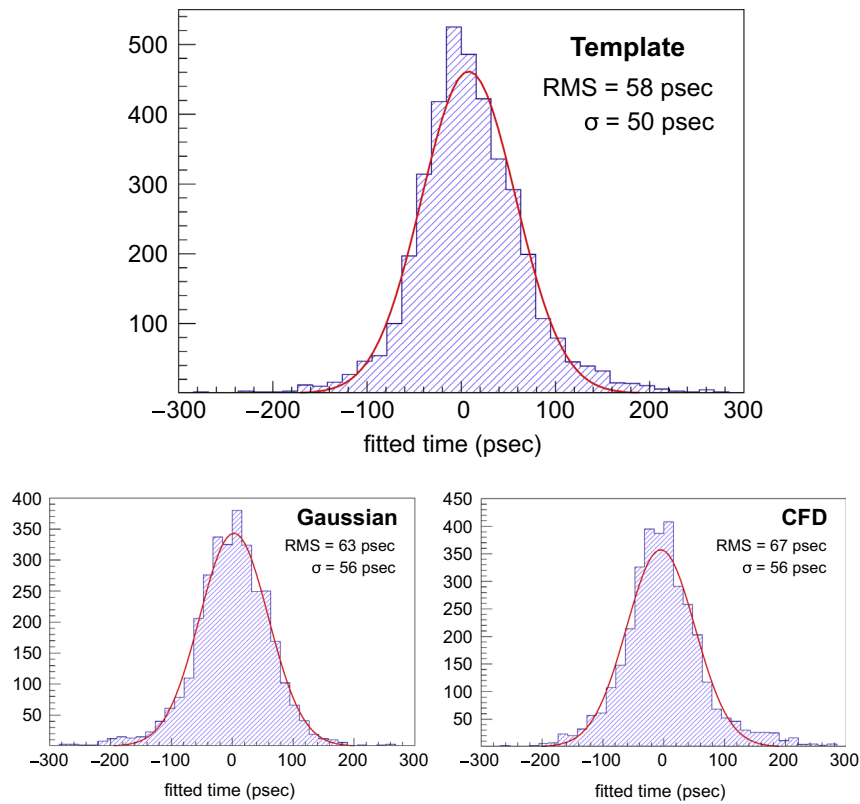


Fig. 9. The single-PE transit-time spread measured for the LAPPD™ stack inside the 8 in. chamber, derived using the three different fit methods (see text). Top: using the template fit method. The RMS of the distribution is 58 ps; the sigma of the fitted Gaussian is 50 ps. Numerically integrating the distribution, one finds that 68% of all events fall within ± 47 ps. Lower left: using the gaussian fit method. The RMS of the arrival times is 63 ps, and the fitted sigma is 56 ps. Lower right: using the CFD algorithm. The RMS of the arrival times is 67 ps, and the fitted sigma is 56 ps. Given the inherent limitations of these fit methods, the non-Gaussian character of the reconstructed TTS and wider tails compared to the template fit are expected.

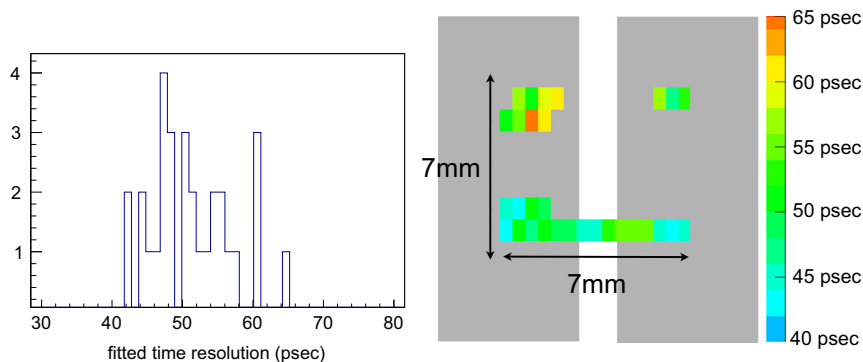


Fig. 10. Left: a histogram of the fitted sigma of the TTS measured at 30 points over a 7 mm by 7 mm square. The mean value of the fitted time resolution is 51 ps, and the RMS from measurement to measurement is 6 ps. Right: a plot showing the locations and values of each measurement, relative to the stripline pattern. The color scale represents the range of measured time resolutions. (For interpretation of the references to color in this figure caption, the reader is referred to the web version of this paper.)

simple CFD methods. However, the pulses can be well approximated by a Gaussian function from the rising edge to a point, slightly past the peak of the pulse.

This method is implemented in two steps. First, we fit the pulse peak with a Gaussian to determine the peak time. Next, using the fitted peak as a reference, we define a fit range and apply a Gaussian fit along the rising edge. This give results close to those of the template fit but is less robust, with a higher failure rate for slightly misshapen pulses.

The most robust method for extracting pulse arrival times is to fit the MCP pulses with a data-derived template waveform. Templates are created by selecting pulses, using a stringent pulse

quality cut, and averaging them together. In some instances this process was repeated a second time, where the fitted time using the original template was used to line the pulses up before combining them to create a more narrow pulse shape. Since the TTS of the pulses (< 100 ps) is considerably smaller than the typical pulse width ($FWHM < 1$ ns), iterative template-making does not substantially improve the results. Once the template has been created, it is used to fit individual pulses. Pulses are interpolated and shifted by a continuum range of time delays until a χ^2 comparison is minimized over a predetermined range of the template. Fig. 8 shows an example pulse with the result of the template fit overlaid.

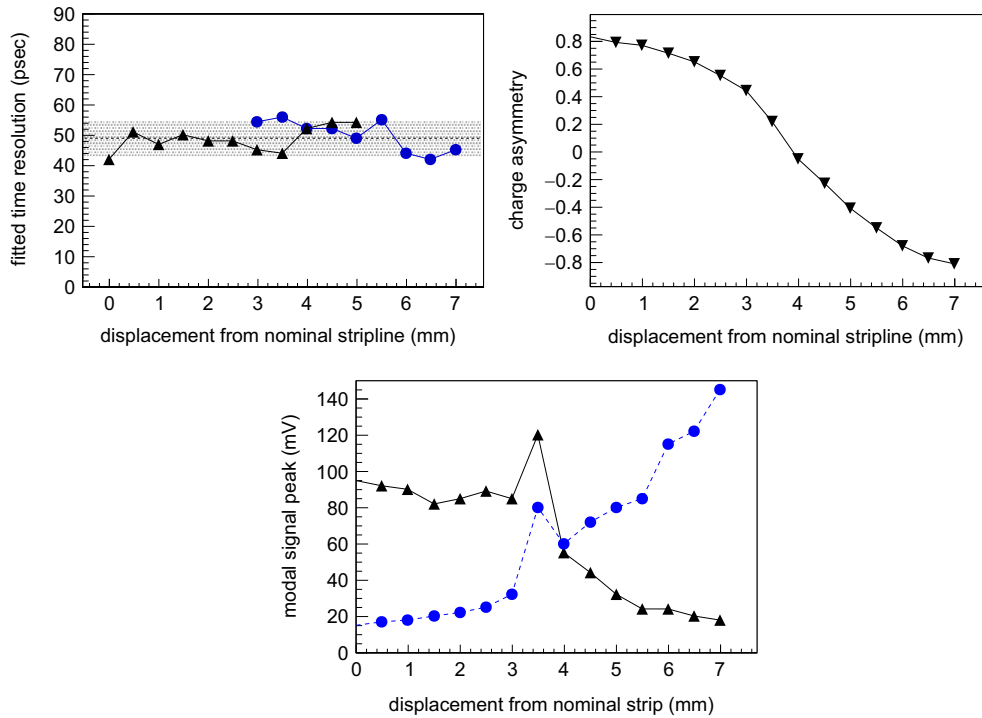


Fig. 11. Upper left: the fitted time resolution as a function of approximate displacement, measured on the nominal stripline (black triangles) and the neighboring stripline (blue circles). The dashed line and shaded band indicate the mean and RMS of the measured resolutions over the scan. Upper right: the asymmetry in charge measured on the two neighboring striplines, plotted as a function of approximate displacement from the nominal strip. An asymmetry of 1 means that all of the charge is on the nominal stripline and -1 means all of the charge on the neighbor. Bottom: the modal signal peak, as a function of displacement from the nominal strip. Black triangles correspond to the peak signal on the nominal stripline and blue circles, the neighboring strip. The spike in signal size at displacement ~ 3.5 mm is not understood, but the fractional signal on each stripline is consistent with the location of the beam.

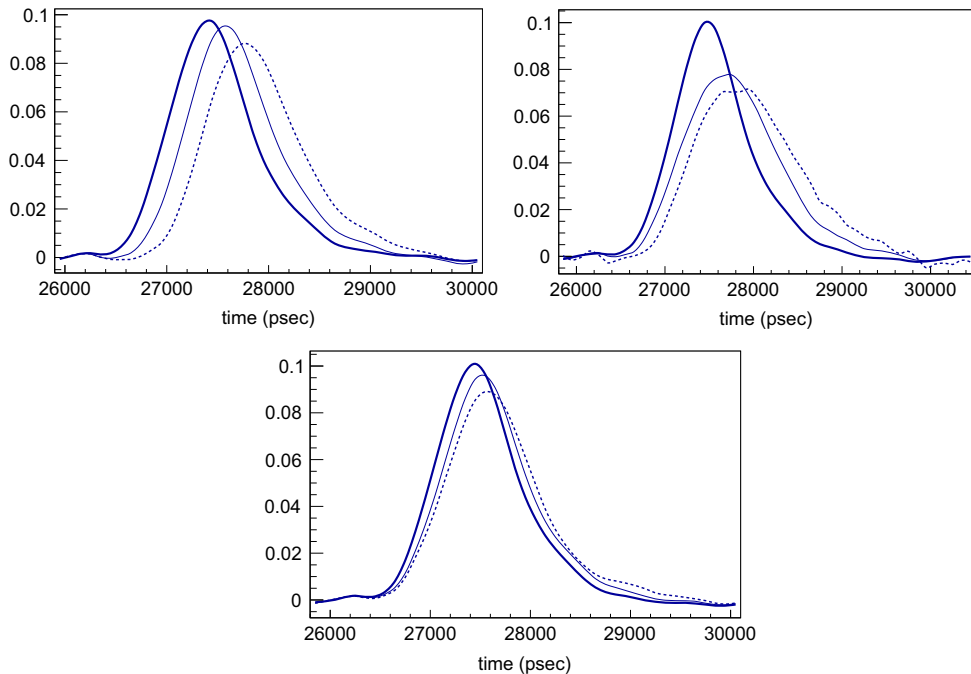


Fig. 12. Upper left: average pulse shape in the 8 in. chamber for three different photocathode voltages: 500 V (thick line), 200 V (thin line), 100 V (dashed), with 1 kV across each MCP, 500 V across the inter-MCP gap, and 400 V across the anode. Upper right: average pulse shape for 500 V (thick line), 200 V (thin), and 100 V (dashed) across the inter-MCP gap, with 400 V across the anode and photocathode. Lower left: average pulse shape for 500 V (thick line), 200 V (thin), and 100 V (dashed) across the anode gap, with 400 V across the photocathode and 500 V across the inter-MCP gap.

7. Results

7.1. The single-photoelectron response

Fig. 9 shows the single-PE transit time spread for pulses produced in the 8 in. chamber, fitted using the template-fit method. The RMS of the distribution is 58 ps and the sigma of the fitted Gaussian distribution is 50 ps. Numerical integration of the TTS finds that 68% of the events fall within ± 47 ps. These observed resolutions are robust, over the choice of algorithm and over the location of the laser beam on the surface of the detector.

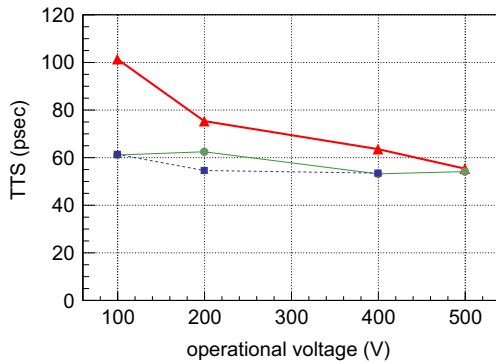


Fig. 13. Transit-time spread of MCPs in the 8 in. chamber, plotted as a function of the key operational voltages: across the gap between the photocathode and top of the first MCP (green circles), between the two MCPs (red triangles), and between the bottom of the second MCP and anode (blue squares). Timing for all gap voltages is preferred to be above 200 V, and performance is most sensitive to the photocathode and inter-MCP gaps.

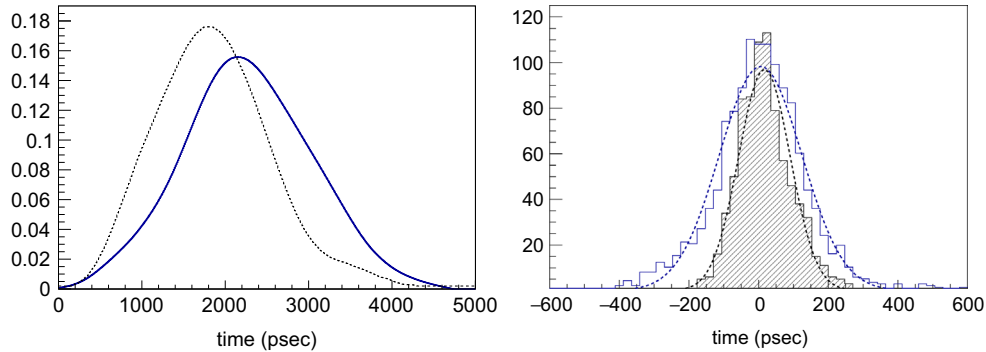


Fig. 14. Left: average pulse shape for 2 different configurations of the demountable LAPPDTM: one with low voltages (< 100 V) across all of the gaps (blue solid line), and one with higher gap voltages (dashed black). Right: the TTS for the two configurations. The high gap-voltage configuration is the shaded black histogram, with $\sigma=78$ ps for the fitted Gaussian (dashed line). The TTS for configuration with low gap voltages is shown by the blue solid line, with a fitted σ of 128 ps.

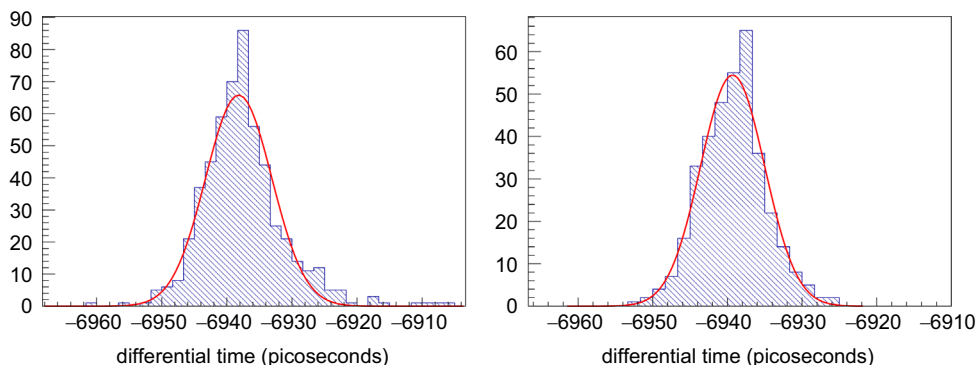


Fig. 15. Left: differential time spread for the demountable detector, fitted with a Gaussian. The RMS of the distribution is 6.4 ps, and sigma of the Gaussian is 5.1 ps. Right: with a modest cut on $N/S < 0.01$, the sample is reduced by only 44%, leaving a DTS distribution with a more gaussian shape with RMS 4.8 ps and fitted sigma of 4.3 ps.

Fig. 9 also shows the transit-time spread reconstructed using the template method, compared with reconstructions using the Gaussian fit and the constant-fraction algorithm. The derived TTS is consistent to within 10 ps, regardless of which of these methods was used.

The absolute time resolution, measured with respect to an external trigger, is dominated by jitter intrinsic to the gain stage. As was discussed in Section 3.1, single-PE jitter from different strike points in the pore should be of order of tens of picoseconds, whereas the anode and digitization are capable of single-ps sensitivity for large signal-to-noise ratios. Thus, the time resolution for single-photoelectrons remains above 40 ps as noise over signal (N/S) approaches zero, in contrast with differential timing, which approaches single picosecond resolutions in the large signal-limit (see Section 7.2).

The spatial uniformity of the time resolution was tested by performing a scan over a $7 \text{ mm} \times 7 \text{ mm}^2$ of the MCP. Fig. 10 shows the fitted time resolution (σ of the Gaussian fit to the TTS) for 30 measurements taken over this area. The TTS was found to be uniform over distances larger than the $O(10) \mu\text{m}$ scale of the capillary structure, and even transitioning from one stripline to the next. The mean resolution is 51 ps, and the RMS from point-to-point is 6 ps. Displacing the beam spot by 7 mm in the direction transverse to the striplines, the peak signal will shift entirely from one stripline to its nearest neighbor. We found that fitting the arrival time on the dominant stripline alone was adequate to obtain single-PE resolutions consistently below 65 ps, even in the region where signal is split between the two striplines (Fig. 11).

The width of the TTS depends on operational voltages, particularly across the gaps between the various stages of the MCP chain. As the gap voltages drop below critical values, the time

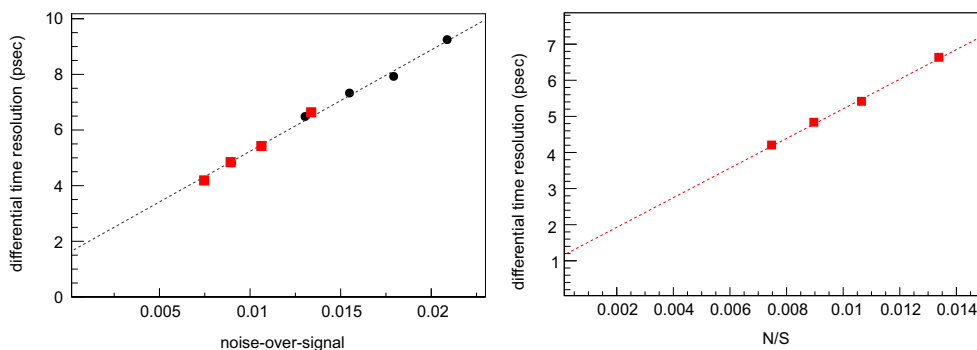


Fig. 16. Left: differential time resolution as a function of noise/signal, plotted for data collected using the Demountable detector in 2014 (red squares) and the 8 in. chamber in 2012 (black circles). Error bars are smaller than the marker size. The intercept of fitted line intersects at 1.6 ps. Right: the same plot, for 2014 demountable data only. The intercept of the fit intersects with 1.1 ps.

resolution degrades. Fig. 12 shows how the shape of the MCP pulses in the 8 in. chamber depend on changes to the three voltages across the gaps in the MCP stack. The most dramatic effects were seen from changes in the voltage across the gap between the two MCPs. Fig. 13 shows the fitted sigma of the TTS as a function of the potential difference across the anode gap, inter-MCP gap, and photocathode gap. Optimal timing was achieved with all of these voltages set above 200–300 V. The dependence was strongest for the inter-MCP gap and photocathode gap, consistent with the observation that this gap had the largest impact on pulse shape.

Similar relationships between gap voltages and time resolution were observed in the demountable detector. In the demountable, we did not originally have access to grid spacers with resistances well matched to those of the MCPs. Consequently, the voltages across all three gaps were below 100 V when the MCPs were operating at full voltage. In a later study, these spacers were replaced with a higher resistance set. Fig. 14 shows the average pulse shape for the demountable with the low resistance and high resistance grid spacers, along side the corresponding TTS distributions. Consistent with observations in the 8 in. chamber, the demountable with low voltages across the gaps delivered time resolutions above 100 ps, while later studies with higher gap voltages demonstrated resolutions below 80 ps.

Further improvements in LAPPDTM single-PE time resolution may be achieved through reductions in pore size [19], and higher yield of the first strike in the pore resulting from higher SEE surface coatings.

7.2. Differential timing and the large-signal limit

Even for single-photoelectrons, the pulse-by-pulse jitter cancels out when one looks at the differential time resolution – jitter in the difference between the arrival of the signal at the two ends of the anode. Differential timing resolution is not limited by the intrinsic properties of the gain stage except inasmuch as they provide large signal. Rather, differential time resolution is limited by the characteristics of the pulse such as the rising edge and size of the pulse, and electronics characteristics such as noise-over-signal (N/S), analog bandwidth, and sampling rate.

The Differential Time Spread (DTS) thus provides a handle on the time resolving characteristics of the detector system, minus those of the MCP stack. It indicates the limiting TOF-resolution for large, multi-photoelectron pulses.

Fig. 15 shows the differential time resolution for single-photoelectrons in the demountable LAPPDTM, operating at 2.7 kV, which corresponds roughly 1.25 kV per MCP. The RMS of the distribution is 6.8 ps. The sigma of the fitted gaussian is 5.1 ps,

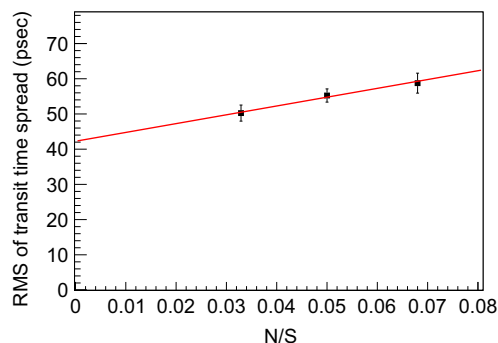


Fig. 17. Single-photoelectron time resolution measured in the 8 in. chamber, binned by noise/signal (2σ error bars). Slight improvements are seen with larger signals, but the single-PE resolutions are limited by fundamental constraints such as pore diameter and asymptotically approach 42 ps for large S/N .

although the shape of the distribution is non-Gaussian. The bell-bottomed shape of the DTS distribution is expected since it is effectively the sum of multiple Gaussians, each corresponding to the resolution for a particular range of pulse sizes. Small pulses have a broader Gaussian, while large pulses are more narrow. Even so, by simply cutting more tightly on the quality of the χ^2 of the template fit we achieve a more Gaussian subset of 66% of the original DTS distribution with an RMS of 4.8 ps and fitted Gaussian of 4.3 ps (shown on the right in Fig. 15). Some of this limiting resolution is due to the finite spot size of the laser beam (~ 0.5 mm), and limitations of the digital readout of the two independent oscilloscope channels used to measure each side of the stripline.

The data sets can be further divided into bins of N/S . Fig. 16 shows the relationship. Even with single-PE data, N/S levels as low as 0.006 were achievable, due to the very high pulse amplitudes of the demountable (see Fig. 18). As expected, pulses with smaller N/S (corresponding to larger signals) demonstrate better time resolution. A linear fit to these points intersects with the y-axis at a resolution close to 1 ps for large signals. In contrast, the single-PE absolute time resolution is dominated by intrinsic jitter in the MCP stack and remains above 40 ps, even in the large-signal limit (Fig. 17). The fluctuations in avalanche formation that dominate the single-PE TTS cancel in the differential timing measurement. This explains the robustness of the relationship between the differential time resolution and N/S , measured with different MCP stacks and at different times.

The measured differential time resolution of 5.1 ps corresponds to a spatial resolution in the direction along the striplines of roughly 0.44 mm. Fig. 19 shows the average time delay between the two ends of a stripline as a function of position along that

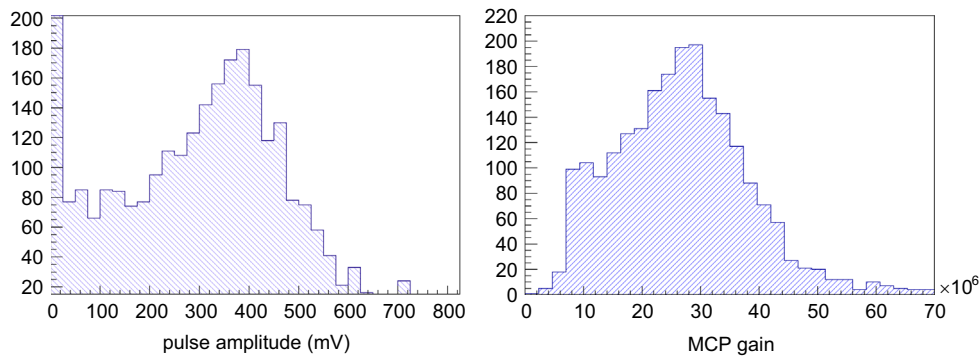


Fig. 18. Left: distribution of signal amplitudes from the demountable LAPPDTM operating at 2700 V, including pedestal events (zero bin). Right: the reconstructed MCP gain distribution for good pulses, with peak at around 3×10^7 .

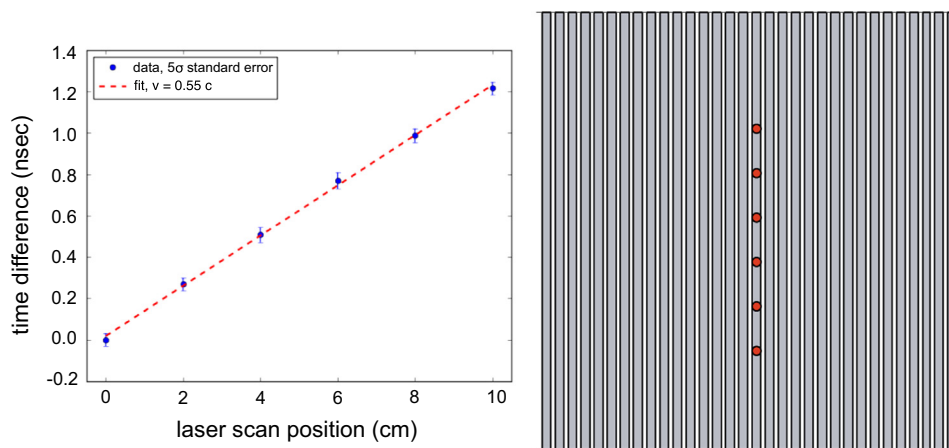


Fig. 19. Mean differential time between the arrival of the pulse at the two ends of the microstripline anode, plotted as a function of position along the anode (left).

stripline. These data show a linear relationship with a slope of roughly $0.57c$, in agreement with the measured speed of signal propagation along the micro-striplines [11].

8. Conclusion

LAPPDTM detector systems are capable of providing absolute time resolutions for single-PEs consistently below 100 ps, and typically below 60 ps. Moreover, the large gain and high signal-to-noise ratio make LAPPD pulses easy to separate from background. While absolute time resolution of single-photoelectrons is limited by intrinsic factors such as pore geometry and operational voltages, differential time resolutions between the two ends of a microstripline are limited largely by the RF characteristics of the low cost, silk-screened glass anode and by the oscilloscope readout. In this paper, we observe differential time resolutions below 5 ps for large signals, with an extrapolated resolution below 2 ps as N/S approaches zero. Further improvements to the gain structure and readout can enable even better single-PE and large signal performance.

Acknowledgments

This work could not have been done without the talent and dedication of Joe Gregar of the ANL Glass Shop, Rich Northrop and Robert Metz of the UC Engineering Center, Mary Heintz and Mark Zaskowski of the UC Electronics Development Group. We thank Harold Gibson and Haidan Wen of the ANL Advanced Photon Source for laser and electronics support at the APS testing lab. We

thank Jeffrey Elam and Anil Mane (ANL), and Neal Sullivan (Arradance) for their critical role in providing the ALD functionalized MCPs used in this paper. We are grateful to Gary Drake for his help in mitigating the electronics noise and Dean Walters with advice on vacuum-related matters. We thank Jason McPhate and Oswald Siegmund for advice and encouragement. Finally, we would like to thank Incom Inc. for providing the 8 in. substrates, technical assistance with glass parts, and helpful discussions. The activities at Argonne National Laboratory were supported by the U.S. Department of Energy, Office of Science, Office of Basic Energy Sciences and Office of High Energy Physics under Contract DE-AC02-06CH11357, and at the University of Chicago by the Department of Energy under Contract DE-SC-0008172 and the National Science Foundation under Grant PHY-1066014. Matthew Wetstein is grateful for support from the Grainger Foundation.

References

- [1] J.L. Wiza, *Nuclear Instruments and Methods* 162 (1979) 587.
- [2] A.S. Tremsin, O.H.W. Siegmund, *Review of Scientific Instruments* 70 (8) (1999) 3282. <http://dx.doi.org/10.1063/1.1149905>.
- [3] J.S. Milnes, J. Howorth, Picosecond time response characteristics of micro-channel plate pmt detectors, 5580, *SPIE* (2005) 730. <http://dx.doi.org/10.1117/12.568180>.
- [4] M. Akatsu, Y. Enari, K. Hayasaka, T. Hokuue, T. Iijima, K. Inami, K. Itoh, Y. Kawakami, N. Kishimoto, T. Kubota, M. Kojima, Y. Kozakai, Y. Kuriyama, T. Matsuishi, Y. Miyabayashi, T. Ohshima, N. Sato, K. Senyo, A. Sugi, S. Tokuda, M. Tomita, H. Yanase, S. Yoshino, *Nuclear Instruments and Methods in Physics Research Section A: Accelerators, Spectrometers, Detectors and Associated Equipment* 528 (3) (2004) 763. <http://dx.doi.org/10.1016/j.nima.2004.04.207>.
- [5] K. Inami, N. Kishimoto, Y. Enari, M. Nagamine, T. Ohshima, *Nuclear Instruments and Methods in Physics Research Section A: Accelerators, Spectrometers, Detectors and Associated Equipment* 560 (2) (2006) 303. <http://dx.doi.org/10.1016/j.nima.2006.01.027>.

- [6] O.H.W. Siegmund, Vacuum Ultraviolet Spectroscopy II, Series: Experimental Methods in the Physical Sciences 32 (1998) 139. [http://dx.doi.org/10.1016/S0076-695X\(08\)60280-X](http://dx.doi.org/10.1016/S0076-695X(08)60280-X) (Chapter 7).
- [7] S.M. George, Chemical Reviews 110 (1) (2009) 111. <http://dx.doi.org/10.1021/cr900056b>.
- [8] S.J. Jokela, I.V. Veryovkin, A.V. Zinovev, J.W. Elam, Q. Peng, A.U. Mane, The characterization of secondary electron emitters for use in large area photodetectors, Application of Accelerators in Research and Industry AIP Conference Proceedings 1336 (2011) 208. <http://dx.doi.org/10.1063/1.3586090>.
- [9] N. Sullivan, P.de Rouffignac, D. Beaulieu, A. Tremsin, K. Saadatmand, D. Gorelikov, H. Klotzsch, K. Stenton, S. Bachman, R. Toomey, Novel micro-channel plate device fabricated with atomic layer deposition, in: Proceedings of the Ninth International Conference on Atomic Layer Deposition [http://dx.doi.org/10.1016/0003-4916\(63\)90068-X](http://dx.doi.org/10.1016/0003-4916(63)90068-X).
- [10] B.W. Adams, A. Elagin, J.W. Elam, H.J. Frisch, J.-F. Genat, J.S. Gregar, A.U. Mane, M.J. Minot, R. Northrop, R. Obaid, E. Oberla, A. Vostrikov, M. Wetstein, Nuclear Instruments and Methods in Physics Research Section A: Accelerators, Spectrometers, Detectors and Associated Equipment 780 (0) (2015) 107. <http://dx.doi.org/10.1016/j.nima.2015.01.034>.
- [11] H. Grabas, R. Obaid, E. Oberla, H. Frisch, J.-F. Genat, R. Northrop, F. Tang, D. McGinnis, B. Adams, M. Wetstein, Nuclear Instruments and Methods in Physics Research Section A: Accelerators, Spectrometers, Detectors and Associated Equipment 711 (0) (2013) 124. <http://dx.doi.org/10.1016/j.nima.2013.01.055>.
- [12] A. Lehmann, A. Britting, W. Eyrich, F. Uhlig, Journal of Instrumentation 4 (11) (2009) 11024. <http://dx.doi.org/10.1088/1748-0221/4/11/P11024>.
- [13] Z. Insepov, V. Ivanov, S. Jokela, M. Wetstein, Comparison of back-scattering properties of electron emission materials, in: Proceedings of the Particle Accelerator Conference, TUP005, 2011, pp. 1–3.
- [14] J.-F. Genat, G. Varner, F. Tang, H. Frisch, Nuclear Instruments and Methods in Physics Research Section A: Accelerators, Spectrometers, Detectors and Associated Equipment 607 (2) (2009) 387. <http://dx.doi.org/10.1016/j.nima.2009.05.193>.
- [15] S. Ritt, The role of analog bandwidth and S/N in timing (talk), in: Workshop on the Factors that Limit Time Resolution in Photodetectors, University of Chicago, 2011, URL https://psec.uchicago.edu/workshops/fast_timing_conf_2011/.
- [16] D. Stricker-Shaver, S. Ritt, B. Pichler, IEEE Transactions on Nuclear Science NS-61 (6) (2014) 3607. <http://dx.doi.org/10.1109/TNS.2014.2366071>.
- [17] E. Oberla, J.-F. Genat, H. Grabas, H. Frisch, K. Nishimura, G. Varner, Nuclear Instruments and Methods in Physics Research Section A: Accelerators, Spectrometers, Detectors and Associated Equipment 735 (2014) 452. <http://dx.doi.org/10.1016/j.nima.2013.09.042>.
- [18] B. Adams, M. Chollet, A. Elagin, E. Oberla, A. Vostrikov, M. Wetstein, R. Obaid, P. Webster, Review of Scientific Instruments 84, 061301, <http://dx.doi.org/10.1063/1.4810018>.
- [19] C. Craven, Incom, Inc, Private Correspondence.